OVERFLOW Analysis of Supersonic Retropropulsion Testing on a Blunt Mars Entry Vehicle Concept

Logan D. Halstrom*
NASA Ames Reseach Center, Moffet Field, CA, 94035

Thomas H. Pulliam† , Robert E. Childs‡ , and Paul M. Stremel§
Science & Technology Corporation, Moffett Field, CA, 94035

Supersonic retropropulsion (SRP) flow over a Hypersonic Inflatable Aerodynamic Decelerator (HIAD) blunt-body vehicle was simulated using the OVERFLOW Computational Fluid Dynamics (CFD) solver. Two nozzle configurations were tested (1E and 1F) as a subset of the seven total configurations in the Descent System Study (DSS) testing campaign. A generalized, Adaptive Mesh Refinement (AMR) shock capturing and plume refinement technique was developed and calibrated for producing automatic and unique grid systems optimized for any given testing condition. Solution independence from grid resolution was determined by successively increasing grid refinement until asymptotic convergence of the mean aerodynamic loads was observed. OVERFLOW Reynolds-averaged Navier-Stokes (RANS) solutions produced realistic SRP flow phenomena, including Mach disk normal shocks contained in high-thrust plumes and bow shock triple-points. Solutions for the 1E nozzle configuration were steady. Conversely, a subset of the 1F test conditions were unsteady and exhibited periodic, non-sinusoidal expansions and contractions of the streamwise-oriented plume, resulting in unsteady aerodynamic loads on the vehicle. Initial investigations into the effect of turbulence modeling fidelity demonstrated significant differences between the aerodynamic loads simulated with RANS and Detached Eddy Simulation (DES). Multiple flow mechanisms were identified as root causes of these differences, including bow shock shape augmentation and reduced entrainment due to reduced turbulence in the DES simulations. Initial comparisons of pitching moment control authority and aerodynamic drag performance between the tested nozzle configurations demonstrated that the 1E configuration may be more advantageous for the Mars Entry, Descent, and Landing (EDL) task.

I. Nomenclature

Symbols

C_A	=	axial force coefficient
C_D	=	drag force coefficient
C_P	=	pressure coefficient
C_T	=	thrust coefficient
C_v	=	thermal energy coefficient
C_{P_0}	=	stagnation pressure coefficient
C_m	=	pitching moment coefficient
L/D	=	lift-to-drag ratio
M	=	Mach number

*Aerospace Engineer, Systems Analysis Office (ARC-AA), AIAA Member, logan.halstrom@nasa.gov
†Senior Research Scientist, Systems Analysis Office, AIAA Associate Fellow.
‡Senior Research Scientist, Systems Analysis Office.
§Senior Research Scientist, Systems Analysis Office, AIAA Member.

Re = Reynolds number
V_{mag} = total velocity magnitude
α = angle of attack

Acronyms

AETC = Aerosciences Evaluation and Test Capabilities
AMR = Adaptive Mesh Refinement
BC = boundary condition
CC = compressibility correction
CFD = Computational Fluid Dynamics
DES = Detached Eddy Simulation
DSS = Descent System Study
EDL = Entry, Descent, and Landing
GCDP = Game Changing Development Program
HIAD = Hypersonic Inflatable Aerodynamic Decelerator
HLLC = Harten-Lax-van Leer-Contact
HLLE++ = Harten-Lax-van Leer-Einfeldt
LUPWT = Langley Unitary Plan Wind Tunnel
NASA = National Aeronautics and Space Administration
QCR = Quadratic Constitutive Relation
RANS = Reynolds-averaged Navier-Stokes
RC = rotation and curvature
SRP = supersonic retropropulsion
SSOR = Symmetric Successive Over-Relaxation
SST = Shear Stress Transport
STMD = Space Technology Mission Directorate
TKE = turbulence kinetic energy
URANS = Unsteady Reynolds-averaged Navier-Stokes

II. Introduction

DEVELOPMENT of the science and technology required to enable human exploration of Mars has been ongoing for decades at the National Aeronautics and Space Administration (NASA) as well as at other organizations and is moving forward at an increasing pace. One of the key remaining technical challenges in active development is the ability to safely and reliably land significantly large payloads on the planet's surface. The Martian atmosphere is tenuous in nature, with a relatively low average density that diminishes the deceleration that can be achieved through traditional aerodynamic drag, but still produces aerothermodynamic heating from which a vehicle must be shielded and creates complex vehicle aerodynamics when retropropulsion is used, requiring active control during descent. Recent NASA robotics missions have successfully employed a four-stage Entry, Descent, and Landing (EDL) approach: a conventional supersonic aeroshell, a super/subsonic parachute, retropropulsion, and finally a sky-crane. This has proven to be a reliable system, but it is complex and has distinct disadvantages for crewed missions. NASA's critical mission requirement for future EDL vehicles is to be able to deliver large payloads on the order of twenty metric tons, which is twenty times greater than current capabilities. These planned, heavy-mass, Mars missions include both precursor robotic and follow-on human landings [1, 2].

Two such vehicle concepts are the low-L/D Hypersonic Inflatable Aerodynamic Decelerator (HIAD) [3] and mid-L/D CobraMRV vehicle [2, 4, 5]. Figure 1 gives examples of the current vision for each of these vehicles. Both concepts are designed for traditional aerodynamic deceleration and guidance in supersonic flight, decelerating from

orbital velocity to $M \sim 2$, at which point supersonic retropropulsion (SRP) is used for final deceleration and landing. The engines are integrated into the vehicle and shielded for initial hypersonic entry, and the nozzle exit planes are exposed for retropropulsion.

(a) Low-L/D HIAD **(b) Mid-L/D CobraMRV**

Fig. 1 Concept Mars EDL vehicles for human exploration missions [1]

The aerodynamics of SRP vehicles are complex and require increased rigor in the Computational Fluid Dynamics (CFD) modeling process in order to provide good accuracy. This paper focuses on the challenges of tailoring the CFD process to accurately represent the essential features of such flows. Principal aspects of the aerodynamic complexity are:

- The vehicle flies through the highly dynamic wake of its own engines' turbulent plumes.
- The bow shock, when present, has back-pressure support from turbulent jets, and thus has the potential to be highly variable in space and time.
- Significant shock losses through a variable shock can induce a highly dynamic post-shock flow that impacts the vehicle; mixed regions of strong normal shocks and weak oblique shocks can dramatically alter the dynamic pressure in the post-shock region.
- Large scale, unsteady dynamics are relatively common.
- Feedback mechanisms between plume and shock are observed.
- Issues like the modeling of turbulence and reacting flows can significantly affect CFD fidelity.
- The Martian atmosphere is poorly modeled by ideal gas laws; specifically, the thermal energy coefficient thermal energy coefficient (C_v) varies significantly with temperature through a typical EDL vehicle shock.
- Physically relevant length scales vary over a range of roughly 10^5, based on $1cm$ scales for near-vehicle plume shear layers and $1km$ for the plumes' furthest extent in low speed flight. Commensurate time scale will exist.

Attention to key details of vehicle aerodynamics is important for obtaining the best possible results, especially for non-conventional vehicles and aerodynamics. The SRP rocket plumes exert a strong influence over the vehicle's aerodynamics, to the point of reducing the body aerodynamic drag (excluding rocket thrust) to negative drag force coefficient (C_D) at certain flight conditions for some vehicle/nozzle combinations. This type of aerodynamic insight is challenging to obtain without utilizing CFD methods. Vehicle flight conditions in the relatively thin Martian atmosphere are practically impossible to replicate in ground test facilities and truly impossible to match in the Earth's atmosphere. The accuracy of CFD methods is, therefore, impossible to validate with experimental data at true flight conditions. Fortunately, supersonic wind tunnel testing in air is a good surrogate for actual flight conditions, as the differences between Earth and Mars atmospheric gas properties are expected to be less challenging than many other issues.

An extensive wind tunnel testing campaign is being conducted under the NASA Aerosciences Evaluation and Test Capabilities (AETC) portfolio office to assess the relative merits of supersonic wind tunnel testing and CFD methods for fulfilling future aerodynamic data-generation needs. A primary criterion is the ability of CFD to provide vehicle aerodynamics data that is "of comparable quality" to that produced by wind tunnel experiments. Ross et al. give a description of the objectives and scope of this effort [6]. One component of this testing campaign is to partner with NASA's Space Technology Mission Directorate (STMD) Descent System Study (DSS) in studying SRP on two concept vehicles: HIAD and CobraMRV. This paper describes the work done to predict the aerodynamics of the HIAD concept using the OVERFLOW CFD solver, and an analogous paper covers the work on CobraMRV with OVERFLOW [7]. Companion papers give an overview of the experiment [8], which will be conducted in early 2022, and the pre-test CFD results simulated with OVERFLOW and several other solvers [9] in preparation for the wind tunnel test.

The current AETC SRP wind tunnel testing effort will run tests for both the low-L/D HIAD and mid-L/D CobraMRV vehicle concepts over a variety of supersonic test conditions with varying levels of engine thrust in the NASA Langley Unitary Plan Wind Tunnel (LUPWT). The final test condition matrix for the campaign includes

seven geometries $\{1A, 1B, 1C, 1D, 1E, 1F, 2A\}$, three freestream Mach number (M)/Reynolds number (Re) conditions $(M, Re/ft) = \{(2.386, 1e6), (3.477, 1e6), (4.568, 1.5e6)\}$, three angles of attack $\alpha = \{0°, 5°, 10°\}$, and four thrust coefficients $C_T = \{0.0, 0.5, 1.0, 2.5\}$. A range of nozzle configurations will be tested on the HIAD in order to investigate the performance effectiveness of nozzle design parameters such as exit area, area ratio, cant angle, and placement location. The resulting 207-case test matrix is summarized in Table 1. For the analysis conducted in this paper, the OVERFLOW CFD solver was utilized to simulate 63 unique test matrix conditions prior to wind tunnel testing, covering a subset of the HIAD nozzle configurations (boxed in Table 1) including the 1E and 1F nozzle configurations and a "power-off", configuration without nozzles, representative of the $C_T = 0.0$ conditions for all HIAD variations. These configurations are compared in Fig. 2. Nozzles 1E and 1F have similar throat, nozzle, and exit geometries, but differ in both cant angle and location.

Table 1 Text condition matrix

Geometry	$1A, 1B, 1C, 1D, \boxed{1E, 1F}, 2A$
$(M, Re/ft)$	$(2.386, 1e6), (3.477, 1e6), (4.568, 1.5e6)$
α	$0°, 5°, 10°$
C_T	$0.0, 0.5, 1.0, 2.5$

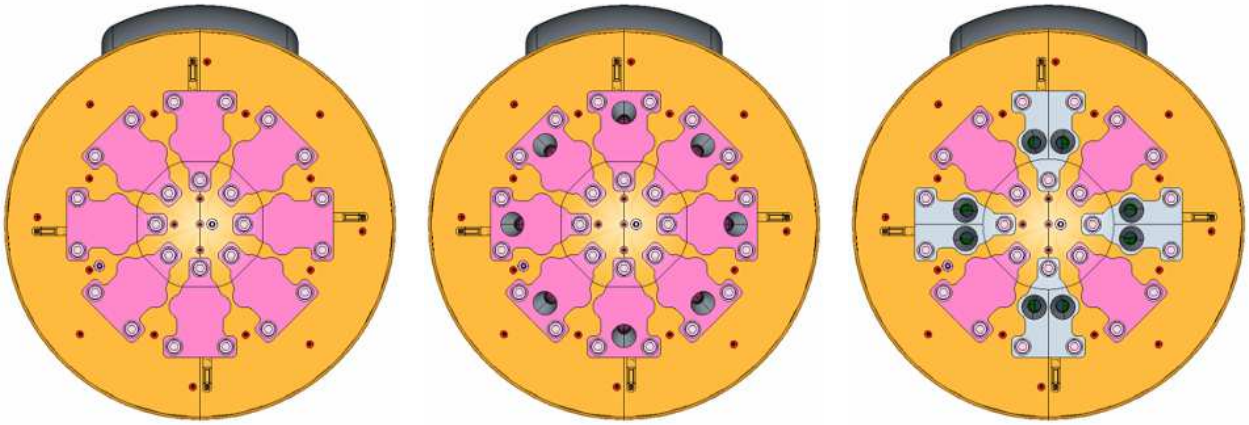

(a) 01 (power-off) **(b) 1E (Radially symmetric, canted 20°)** **(c) 1F (Paired, canted 5°)**

Fig. 2 Nozzle configurations for various DSS HIAD models (Source: Edquist et al. (2020) [10])

Section III of this paper summarizes the CFD solver parameters utilized for the simulations presented in this work. Section IV describes the computational domain of the simulations and the development of a dynamic Adaptive Mesh Refinement (AMR) grid sequencing process for obtaining optimized SRP grids. Section V discusses the SRP flow behaviors observed in the OVERFLOW HIAD simulations, provides a preliminary assessment of the aerodynamic characteristics of the HIAD vehicle, and investigates the dependence of these flow solutions on turbulence modeling methodologies.

III. Computational Methodology

CFD simulations were performed using OVERFLOW, which is an implicit Navier-Stokes solver that employs finite-differencing methods on structured, overset grids [11–14]. Overset grid systems were developed using Chimera Grid Tools (CGT) [15–17] and its associated Graphic User Interface (GUI) Overgrid [16]. Overset region communication, interpolation stencils, and cell blanking were computed using Domain Connectivity Function (DCF) [18, 19].

All solutions were computed using a time-accurate solver with five Newton sub-iterations at each time step to improve convergence. Time step size was determined by successively decreasing the step size until the general unsteady

flow behavior remained consistent between changes, which corresponded to a non-dimensional value of 0.5 for these simulations. Inner-iteration convergence was assessed for each solution to ensure accurate numerics. Time was advanced implicitly using Symmetric Successive Over-Relaxation (SSOR) and with the Harten-Lax-van Leer-Contact (HLLC) upwind spatial discretization scheme employed throughout the tunnel test section and near-body region. Alternatively, the Harten-Lax-van Leer-Einfeldt (HLLE++) upwind scheme was applied locally in the bow shock region to provide more accurate shock capturing.

The two-equation Shear Stress Transport (SST) Reynolds-averaged Navier-Stokes (RANS) turbulence model [20] was employed in the SRP calculations, as it has been shown to be more accurate than other models available in OVERFLOW for flows with rocket plumes and other significant non-wall-bounded shear layers. Much of this type of work was done on the Orion Launch Abort Vehicle and re-entry crew module, for which extensive experimental data was available for model validation [21, 22]. Additionally, specific model options were found to be very important in obtaining the best possible CFD accuracy. For the underexpanded rocket plumes in SRP work, it was found that enabling the rotation and curvature (RC) option and disabling the compressibility correction (CC) option was a superior choice, which is counter-intuitive, as high-Mach number flow generally benefits from the CC option. This superior combination of RC/CC explicitly depends on some error cancellation: the RC model often predicts insufficient shear layer growth in the barrel-shaped shear layers of underexpanded plumes, so disabling the CC model helps compensate for that deficiency, in our aggregate experience. This choice is not suitable for all high speed jets, but works well for the underexpanded ones in these flows. It was also found that the Quadratic Constitutive Relation (QCR) model [23, 24] is beneficial in corner regions of the wind tunnel but has adverse effects in plumes. Again leveraging OVERFLOW's ability to permit the use of different model options on different grids, QCR is applied to the grids that carry the bulk of the wall flow, including its corners, but QCR is disabled in all grids near the vehicle. Additional detail on DSS SRP solution sensitivity to the OVERFLOW solver parameters discussed above can be found in the companion paper by Matsuno et al..

IV. Overset and Adaptive Mesh Methodology

This section describes the main overset grid system comprising the wind tunnel test section, HIAD vehicle model, and wind tunnel sting (see Fig. 6), and it introduces the strategy developed for using AMR to capture and refine the SRP flow.

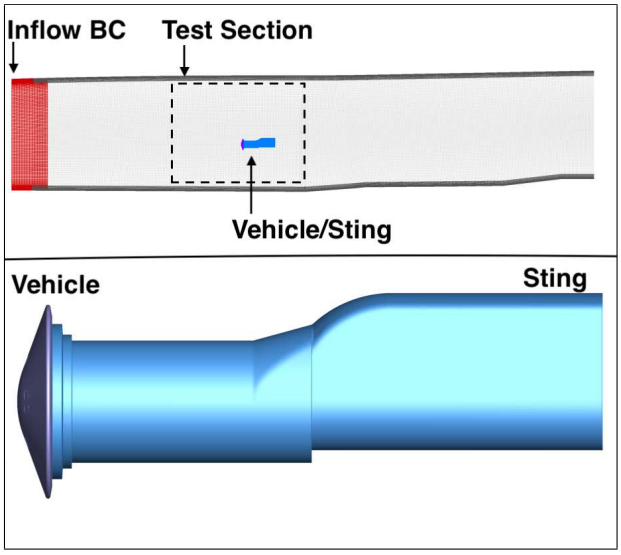

(a) Wind tunnel test section boundary conditions and vehicle surface geometry

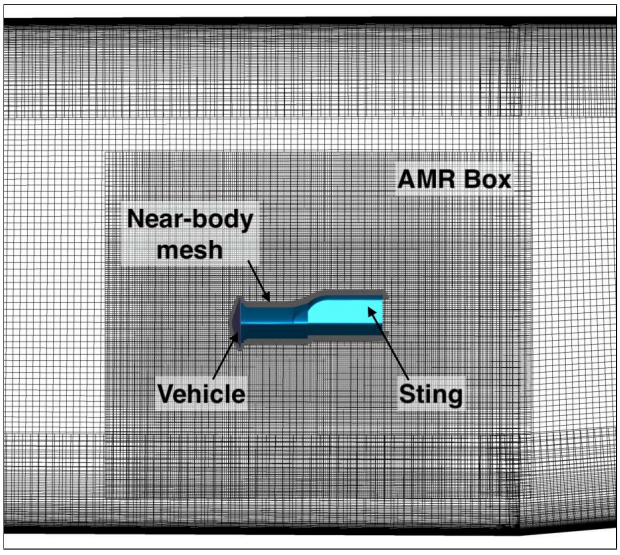

(b) Near-body volume grid and overlaid shock/plume refinement box

Fig. 3 HIAD/LUPWT overset grid system for OVERFLOW SRP simulations

A. Overset Grid System

The overset grid system for the CFD simulations conducted for this work consists of a segment of the LUPWT geometry containing the test section and the HIAD vehicle mounted to a truncated representation of the wind tunnel sting, as depicted in Fig. 3. The inflow boundary condition (BC) to the test section grid is derived from a simulation of the "full-empty-tunnel" geometry and is prescribed at the constant-x plane indicated in Fig. 3a, which is twenty heatshield diameters forward of the vehicle model. Exit flow is modeled over an additional twenty-two diameters through the aft geometry of the wind tunnel test section, which contains two pressure-recovery compression ramps. The vehicle and sting near-body volume grids are encompassed in a surrounding coarse box grid, within which AMR is activated to precisely refine the mesh on which SRP flow features like the rocket plumes and bow shock are computed.

In initial simulations with the LUPWT geometry, it was found that the test section flow cannot be idealized by neglecting the inflow boundary layers and subtle nonuniformity of the true test section flow. The upwash angle of the flow due to the upstream asymmetric wind tunnel nozzle-block expansion was shown to be as great as one degree in magnitude, and there are also weak, wake-like features from hardware in the settling chamber that survive passage through the wind tunnel nozzle-block throat and influence the test section flow. Thus, the inflow BC to the test section for use in the DSS vehicle CFD work was obtained from simulations of the "full" wind tunnel geometry with an empty test section, which were performed by several groups in the AETC effort, including calculations done with OVERFLOW [25]. That which is referred to as the full-empty-tunnel takes its inflow at the approximate location of the start of the settling chamber, which coincides with the last set of turning vanes. This is approximately thirty feet upstream of the start of the wind tunnel nozzle-block contraction. The settling chamber CFD geometry contains all features approximately larger than one inch in size and specifically includes two recessed access port-holes, associated steps, and a "T"-rail, which helps to retain the sliding nozzle-block used to vary the test section Mach number. In the full-empty-tunnel OVERFLOW simulations, the grid system was constructed to have a single high-resolution "BC-grid" plane spanning the entire test section at a fixed streamwise location. The full-empty-tunnel CFD results were recorded on this grid and then used as the inflow BC on the corresponding BC-grid in the test-section-only grid system used to bound the DSS vehicle simulations. The full-empty-tunnel CFD solutions were unsteady at all flow conditions due to flow separation at the access ports and the steep leading edge of the sliding nozzle block. Instantaneous "frames" of the CFD solution were recorded on the BC-grid and were averaged to produce the steady inflow BC for the test section. Thus, the test section inflow for this study is a steady average of the CFD approximation of the true flow in the test section.

B. Grid Refinement Study

When running preliminary simulations for this vehicle, it was determined that aerodynamic loads were dependent on the accuracy of the plume expansion prediction of the CFD solution, which was, in turn, dependent on the mesh resolution. Successive refinement of the AMR box grid was used to refine the solution of the bow shock [26] and to determine grid-independence of the plume solution. Convergence was assessed by observing changes in the time-accurate aerodynamic loads, as depicted in Fig. 4.

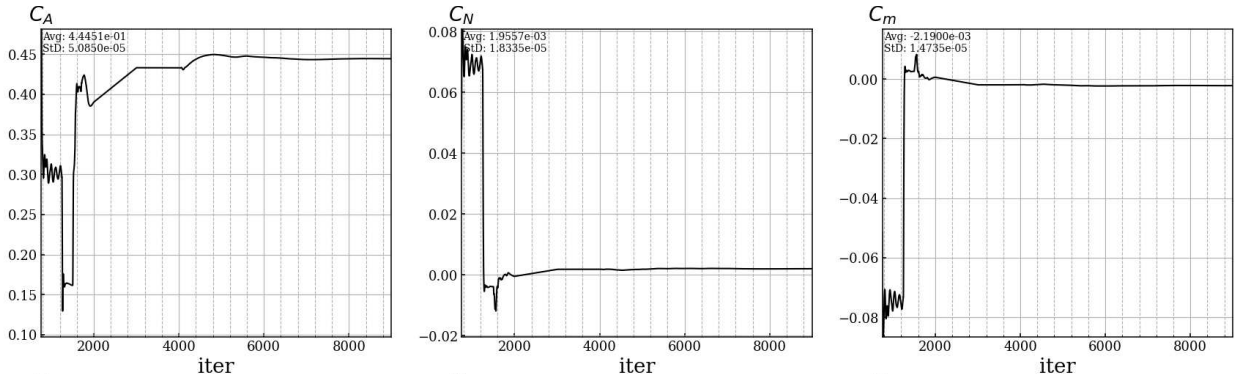

Fig. 4 Force and moment asymptotic convergence history with successive AMR doubling of mesh fineness at 1500, 2000, and 4000 iterations

Four levels of mesh refinement were tested, each level of which permitted grid cells in the AMR region to halve in size based on local gradients in flow parameters. In Fig. 4, loads convergence prior to 1500 iterations represents flow

initialization on the level-one coarse/unadapted grid. The second level of refinement was initiated at 1500 iterations, the third at 2000, and the fourth and final at 4000. The magnitude of the change in heatshield axial force coefficient (C_A) was observed to decrease with each level of refinement, until the change became small enough to consider the solution grid-converged. In the provided example, the percent differences in C_A due to each successive grid refinement were: 36.7%, 4.9%, and 3.5% for the second, third, and fourth AMR levels, respectively, with diminishing returns after the 4^{th} level.

The significant increments in the mean integrated aerodynamic loads due to grid refinement observed in Fig. 4 can be attributed to the resolution of fundamental flow features like the Mach disk in the high-thrust plumes. Fig. 5 shows two OVERFLOW solutions on a coarse and a fine grid for the same test condition using identical solver settings. The grid cells in the plume adaption box in Fig. 5b have been refined to one half the size of their counterparts in Fig. 5a. This level of increased grid resolution allows the solver to identify and resolve the inflection point where the plume oblique shock transitions into a normal shock or Mach disk.

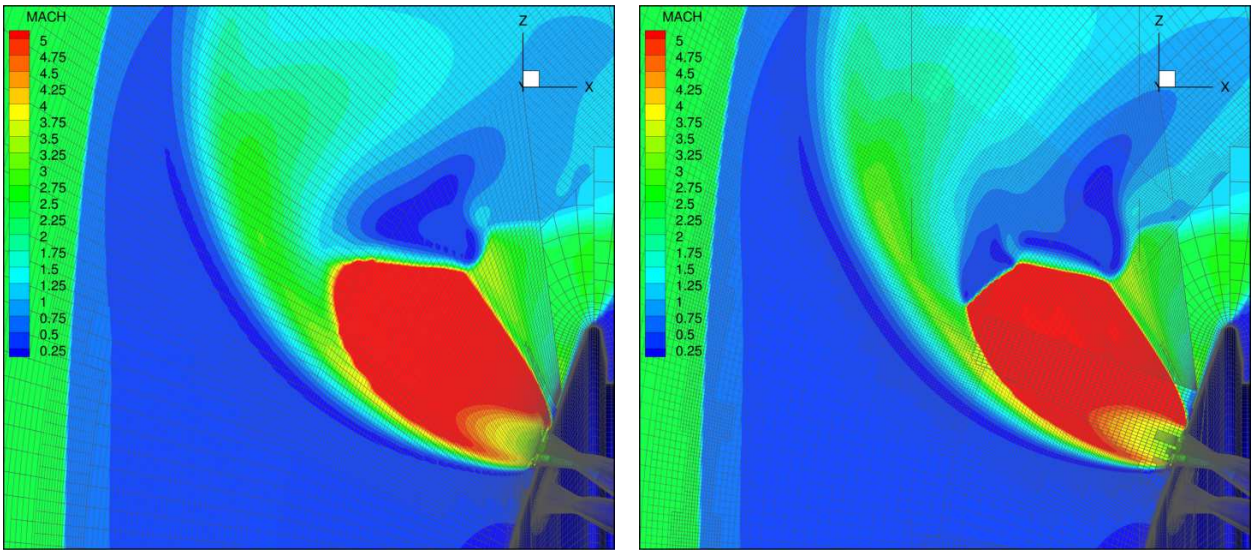

(a) 3 Levels of refinement (oblique shock only) **(b) 4 Levels of refinement (Mach disk resolved)**

Fig. 5 Enhanced refinement of the plume-capturing grids results in Mach disk (SRP plume expansion solution for HIAD 1E at $M = 2.4, C_T = 2.5, \alpha = 0°$)

C. Adaptive Mesh Plume Refinement Strategy

Even more so than typical supersonic blunt-body flows, SRP flows exhibit an extreme variance in the shape and location of the bow shock due to the complicated interaction of the shock and the plumes. Initially, the OVERFLOW HIAD SRP grids were designed with "bespoke", or custom-made, plume and shock refinement boxes for each flight condition to capture these variations, shown in Fig. 6a as a $y = 0$ slice of a revolved "C"-grid. However, the process for generating these grids was tedious and iterative, and the final grid system was often a compromise between optimal designs for different conditions. Through testing and comparison, it was found that a more optimal and efficient approach was to remove the bespoke refinement boxes entirely and, instead, capture the shock and plume system using AMR on a large surrounding box grid (Fig. 6c). This technique has the advantage of both eliminating the guesswork of predicting the location of the bow shock and size of the plume expansion as well as providing an adapted grid that is optimally refined for the specific flight condition. Comparison of the bespoke plume refinement grid and generalized grid adaption solutions in Figs. 6b/ 6d demonstrates similar resolution of SRP flow features, confidently establishing that the automated AMR approach produces consistent flow solutions.

The effectiveness of generalized AMR shock capturing and plume refinement can be observed in Fig. 7, which demonstrates the significant variation in bow shock and plume shape and location between thrust conditions. The figure shows that AMR is effective in detecting these variations and providing appropriate grid refinement in the regions of interest. An added benefit of the generalized AMR technique is a reduction in the total number of grid points in a solution, as AMR only refines the adaption box in regions with significant gradients, improving the overall efficiency of the solution.

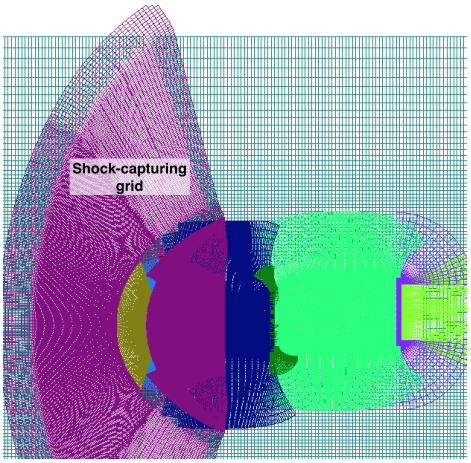

(a) Bespoke grid system (base mesh resolution)

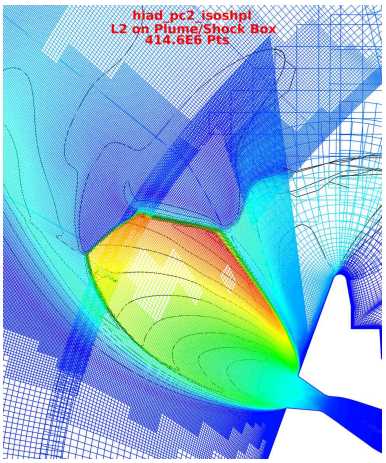

(b) Mach disk solution on bespoke grid with AMR

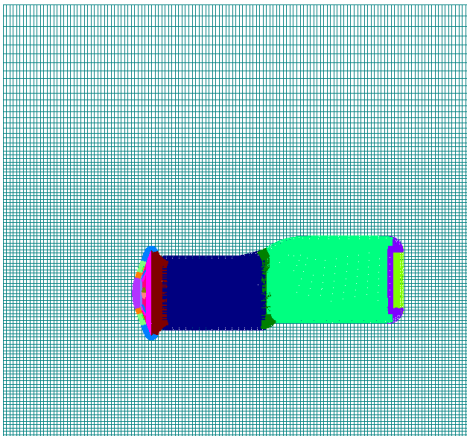

(c) Generalized grid system (base mesh resolution)

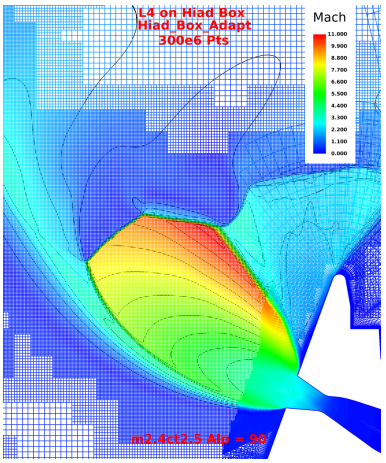

(d) Mach disk solution on general grid with AMR

Fig. 6 Comparable SRP flow solutions between a bespoke grid system manually tuned to the specific flow condition and the generalized, adaptive shock/plume capturing approach

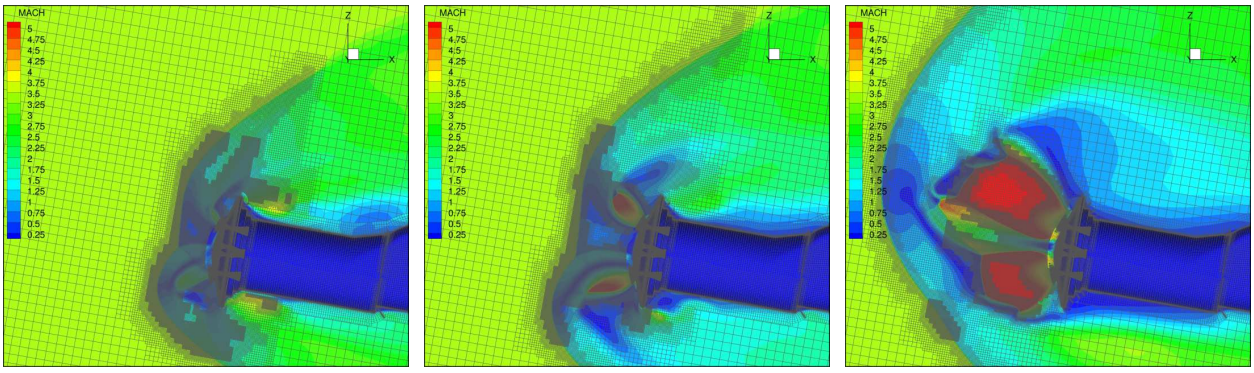

(a) **Low thrust** ($C_T = 0.5$) (b) **Medium thrust** ($C_T = 1.0$) (c) **High thrust** ($C_T = 2.5$)

Fig. 7 Performance of generalized plume adaption box at multiple thrust conditions for HIAD 1F ($M = 3.5, \alpha = 80°$)

V. Pre-Test CFD Results

This section reports the pre-test, OVERFLOW CFD results for the HIAD 1E and 1F configurations. It discusses the aerodynamic phenomena specific to this SRP flow, highlights the unsteady flow behaviors observed for a subset of the flow conditions and geometries, demonstrates solution variation between different turbulence modeling methodologies, and provides an initial assessment of the theoretical EDL performance capabilities of the simulated HIAD vehicle.

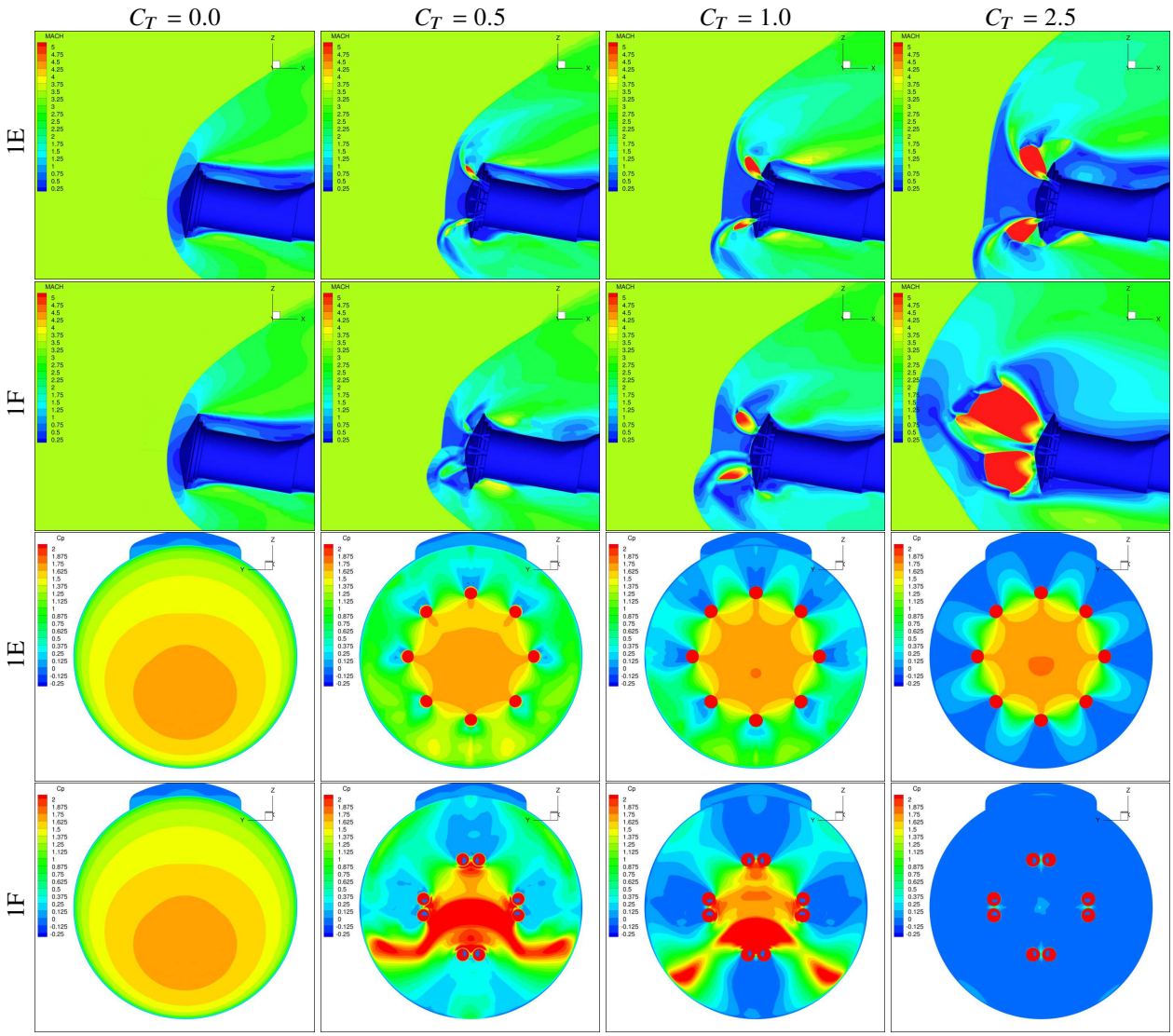

Fig. 8 Instantaneous $y = 0$-plane Mach number and heatshield surface C_P distribution for both models at $M = 3.5, \alpha = 10°$ as a function of thrust coefficient

A. Aerodynamic Characteristics

This section focuses on aerodynamic trends as a function of the independent database parameters: angle of attack (α), thrust coefficient (C_T), Mach number (M). Figure 8 depicts the shock-plume interaction and resulting heatshield surface pressure distribution over both HIAD configurations for various C_T's at a single angle of attack $\alpha = 10°$ and tunnel freestream flow condition $M = 3.5$. In the figure, engine thrust increases left to right, with the left-most column corresponding to the power-off or drag-only condition (which is identical for the 1E and 1F configurations as it is simply the Outer Mold Line of the HIAD vehicle with no engine nozzles). The power-off condition exhibits the typical convex bow shock expected to develop over a supersonic blunt-body. As C_T is increased, the bow shock is pushed forward and

augmented into a concave shape by the nozzle plumes, and a shock triple-point also occurs for non-zero α. Plume expansion is relatively similar between nozzle configurations for all thrust conditions except the maximum $C_T = 2.5$, where the 1F plumes are significantly underexpanded, returning the bow shock to a convex shape.

Nozzle location has a significant effect on heatshield pressure distribution. In the lower left of Fig. 8, we see the baseline surface pressure distribution of a symmetric blunt-body, with diminishing pressure contours centered about the stagnation point. For the power-on cases, the pressure distribution is augmented near each nozzle by impinging high-speed flow from the plumes. The radially symmetric nozzle distribution of the 1E configuration results in a more distributed pattern of these plume pressure "shadows". Conversely, the 1F configuration produces concentrated regions of high-speed flow between nozzle clusters, resulting in an oscillating stagnation region that is not radially symmetric. At the highest thrust condition, the plumes have propagated the bow shock further upstream, causing the surface pressure distributions to appear more symmetric and, in the case of model 1F, reducing the distribution to nearly freestream pressure across the majority of the surface.

Figure 9 demonstrates the variation in plume expansion behavior for the 1F nozzle configuration at the tunnel condition $M = 3.5$, where columns to the right represent increasing engine thrust and descending rows represent increasing α. The shock triple-point only occurs for low and medium thrust conditions at non-zero α and corresponds to conditions with bulk unsteadiness in the SRP solution, as discussed in detail in the following section.

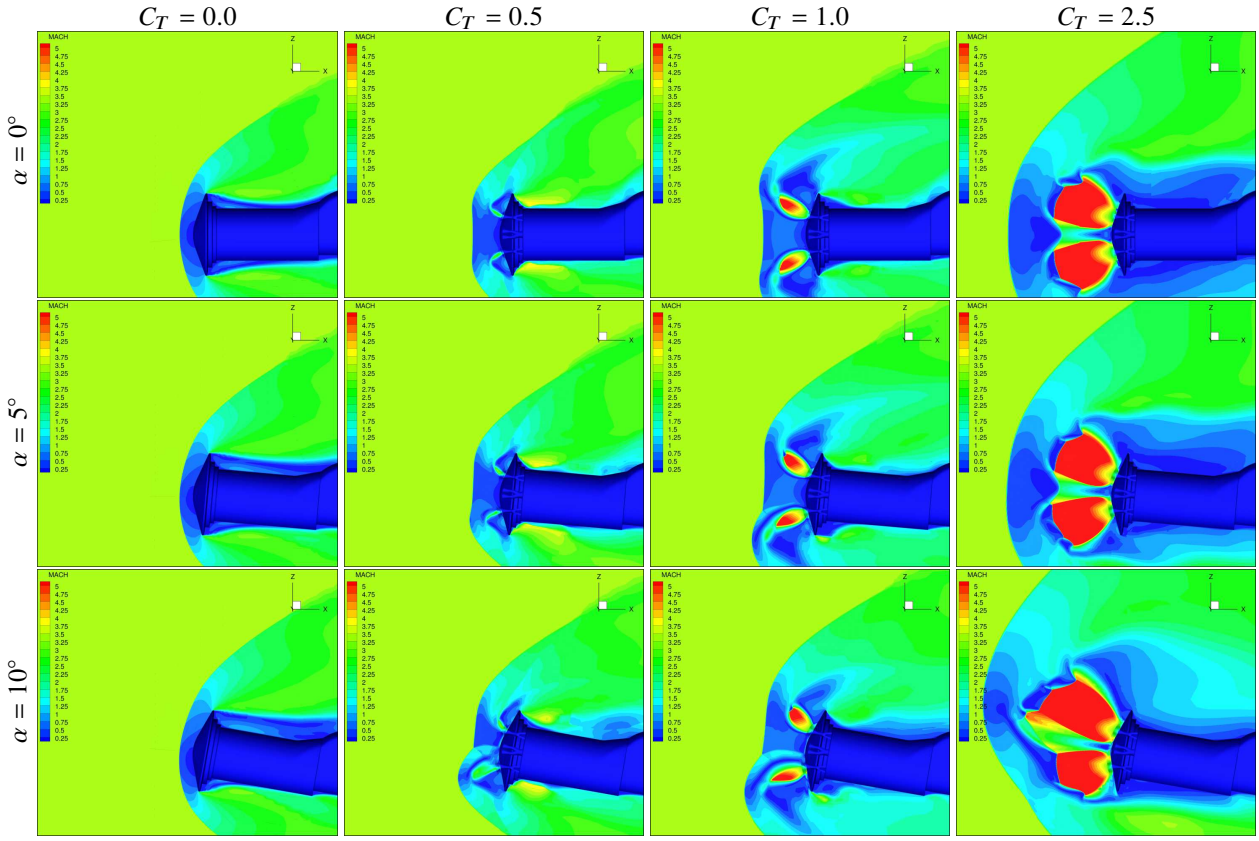

Fig. 9 Mach number contours for HIAD 1F at $M = 3.5$ as a function of angle of attack and thrust coefficient

B. Unsteady Flow Characteristics

The HIAD 1F nozzle configuration is particularly prone to unsteady oscillations at conditions with higher freestream Mach number, lower thrust, and non-zero angle of attack. The unsteady flow phenomena consist of a shifting of the shock triple-point location (depicted in Fig. 10) due to a periodic expansion/contraction of the plume from the most streamwise-aligned lower nozzle cluster. The effect on the aerodynamic body is a gross shift in the stagnation region's shape and location, leading to significant variation in the drag, lift, and pitching moment coefficient on the vehicle over

time. The nature of this oscillation is a cyclic, non-sinusoidal "chugging", with a frequency of $315Hz$, as shown in Fig. 11. Qualitative comparison to past SRP experiments [27, 28] with simple geometries show that this phenomenon is realistic, but experimental data for this specific SRP flow is required to determine the extent of the accuracy of this prediction.

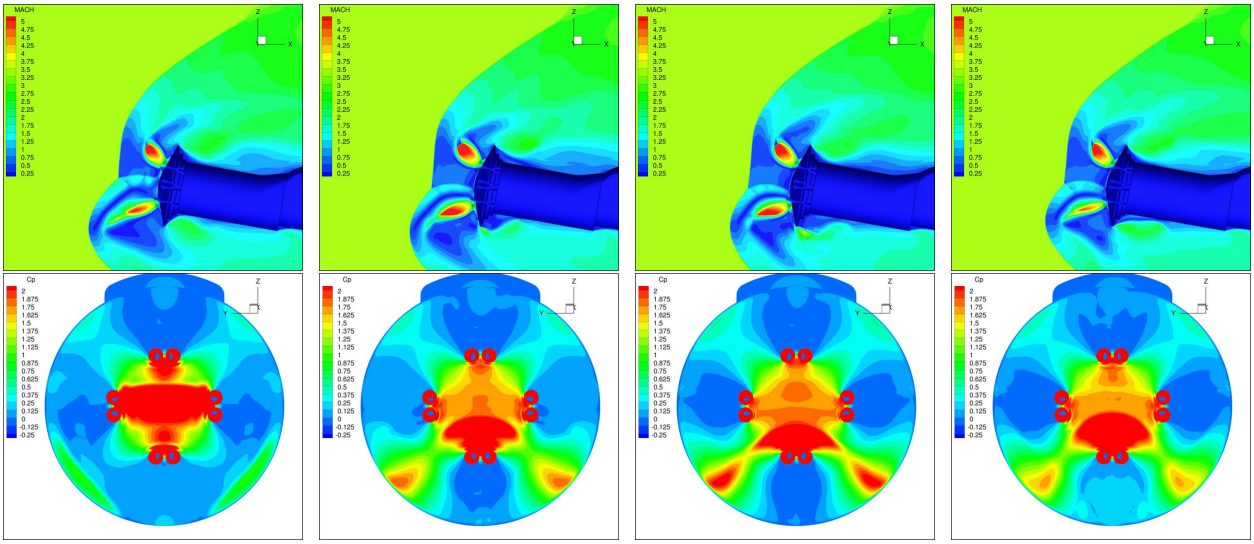

(a) Steady portion (12500) **(b) Plume expansion** (15000) **(c) Peak oscillation** (16000) **(d) Plume contraction** (18000)

Fig. 10 Time-varying, "chugging" plume oscillation of HIAD 1F ($M = 3.5, C_T = 1.0, \alpha = 10°$), ordered by time step corresponding to Fig. 11

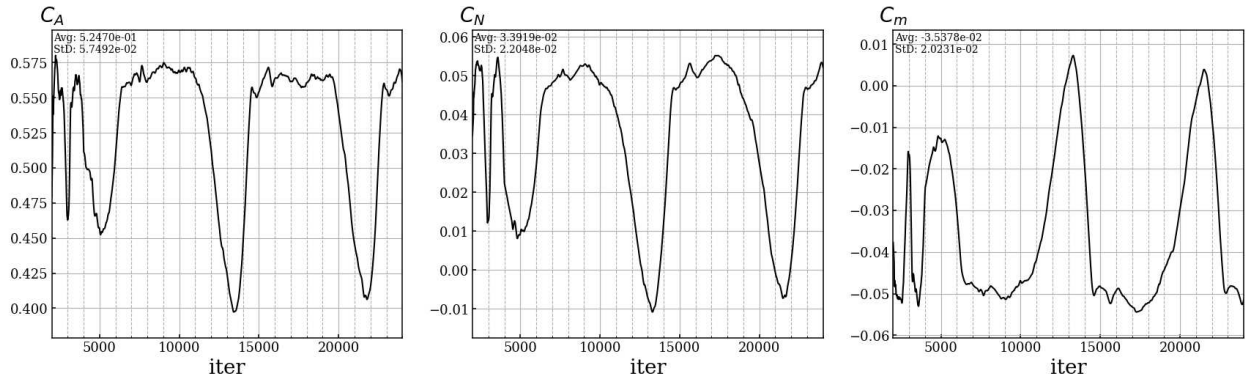

Fig. 11 Unsteady force and moment history of HIAD 1F ($M = 3.5, C_T = 1.0, \alpha = 10°$)

C. Sensitivity to Turbulence Modeling Fidelity

SRP flows present several significant challenges to producing high quality CFD results, including complex, unsteady shocks and plumes, and other phenomena for which turbulence modeling is particularly prone to error. All CFD solvers in the AETC effort predict unsteadiness for at least some flight conditions [9]. Flows with large unsteadiness can, in principle, be computed with time-accurate Unsteady Reynolds-averaged Navier-Stokes (URANS) methods, but Detached Eddy Simulation (DES) is viewed as a very promising higher-fidelity approach for such flows. The OVERFLOW work in this paper has focused on time-accurate RANS calculation, with the SST model and various model options. As part of an initial investigation into the differences between RANS and DES turbulence modeling results for this SRP flow application, a few pilot simulations have been run with DES, at the higher C_T's. The resulting mean loads differ

significantly from those computed with RANS, as depicted in Fig. 12. In addition, the DES simulations result in a more active unsteady oscillation of the SRP plumes, especially in the shock-plume interaction region. Until wind tunnel and realistic flight tests are performed, the relative merits of these turbulence modeling strategies are not known, but, for now, they can inform the uncertainties in the predictions.

The pilot OVERFLOW simulations were run using DES applied to the SST turbulence model. The same dynamical AMR process and limit on the total grid size (250–300 million points) was used for RANS and DES. The time step was typically $0.42e-6$ seconds for DES, and $4.2e-6$ seconds for URANS. The DES simulations were generally initialized from an existing RANS solution by enabling the DES modeling option in the solver, reducing the time step, and allowing the time-accurate flow solution to develop for a significant number of time steps until quasi-steady, repeating flow behavior was observed. This section addresses the causes of the increased C_D/C_A seen in DES solutions, with the goal of informing the experiment design in order to acquire data that can accurately discern the merits of RANS and DES modeling. Three possible mechanisms are discussed here that may affect the pressure on the heatshield and thus C_D.

1) The bow shock in the DES solution is more oblique over enough of the area of the bow shock to give a significantly higher averaged post-shock stagnation pressure. Changes in shock shape are primarily due to differences in how the plumes 'push' on the aft surface of the shock, which further depends on plume shape and spreading rate. Shock dynamics may effect post-shock stagnation pressure, as shock-losses are nonlinear with respect to flow velocity.
2) DES solutions intrinsically capture the role of turbulence kinetic energy (TKE) in the normal stresses and the conversion between TKE and pressure. Unsteadiness is expected as SRP vehicles are flying in the wake of complex plume/shock interactions. Current RANS solvers are less likely to account for the TKE in the total energy equation and will potentially suffer from inaccuracy when this energy-exchange mechanism is significant.
3) The mechanism of blockage versus entrainment by the jet plumes of the incoming flow as it travels radially outward from the stagnation region and off of the heatshield. Blockage tends to trap the incoming flow on the heatshield, lower its outflow velocity, and thus cause higher heatshield pressure, while entrainment ejects this inflow and reduces the pressure.

These mechanisms may be quantified in CFD and experiment, with varying levels of ease and accuracy. Stagnation pressure, TKE, and the role of TKE in the total energy budget are easily evaluated in CFD, and the data processing needed to assess shock dynamics and downstream stagnation pressure in CFD is expected to be challenging, but feasible. None of these quantities are easily measured in experiments focused on full-vehicle aerodynamics, such as in the AETC work, but other metrics can be used for comparison between simulation and experiment. Shock dynamics can be observed with high-speed video of CFD and experiment. Blockage increases are correlated with the size of the plumes, which is a geometric feature that can be observed in CFD and experiment. Increases in the flow entrainment are similarly correlated with the combination of shear layer growth rate and jet velocity and can be thought of as the normal-velocity inflow to a shear layer, but are not easily measured in either CFD or experiment.

Understanding which of these mechanisms are dominant is relevant, as CFD with RANS or DES has different accuracy and cost characteristics for these mechanisms. First, consider the near-field plume shear layers; the first barrel-shock cell in the jet plumes, for example. Good accuracy is needed for the shape of and the entrainment into the jets' shear layers. RANS and DES should give similar accuracy for the 'inviscid shape' of the plume. In the authors' current experience, RANS has limited accuracy for turbulence and entrainment, and DES has even less accuracy until *significant* computational effort is expended. With fifth-order spatial discretization, as OVERFLOW is typically used for DES, roughly 50 grid points across a shear layer are required, with nearly isotropic grid spacing, for good resolution of the fluctuating vortical flow structures of turbulence. None of the current AETC simulation efforts have yet approached this level of resolution, including the present. Conversely, the downstream development of plumes, as they are distorted by the interaction with the external flow, is easier for DES to simulate, as the dominant length and time scales are larger and more easily resolved. However, the plumes' near-field accuracy likely affects the downstream simulation, with the potential to degrade the overall accuracy. Dynamics of the bow shock and the interplay of TKE and pressure in the energy equation are predicted by DES, but not by RANS. Thus, DES has the potential to give superior accuracy, but only after the challenging task of properly tuning the solver and computational domain.

Figure 12 gives the C_A on the heatshield for the RANS calculation, followed by a restart with DES modeling. The switch to DES modeling is evident in the onset of unsteadiness and an increase of $\Delta C_A \sim 15\%$ in the mean C_A. The DES run is long enough to capture more than ten periods of an apparent dominant cycle, but there are also cycle-to-cycle variations that indicate lower frequency content that is potentially present but not fully-resolved in the current solver convergence period. Still, the presented results represent sufficient time-asymptotic convergence to accurately discriminate between the aerodynamics mechanisms predicted by RANS and DES. It should also be noted

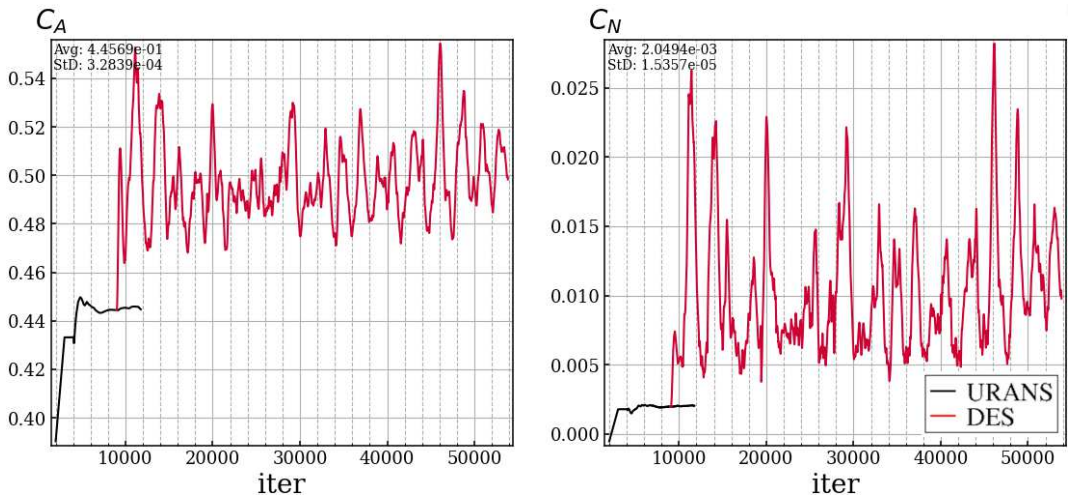

Fig. 12 Time histories of the HIAD vehicle heatshield aerodynamic loads demonstrating a significant difference in the mean aerodynamic force on the vehicle between simulations using URANS and DES turbulence modeling techniques ($M = 2.386$, $\alpha = 10°$ **and** $C_T = 2.5$)

that this mean load increment between turbulence modeling techniques was not universal across all of the pilot DES cases, so the relative merits of each methodology may vary between specific flow conditions.

Figure 13 gives time-averaged flow field data relevant to the mechanisms noted in the discussion above. Time averaging of the flow solutions was computed over sufficiently large time intervals to accurately represent mean aerodynamic trends; 100 time steps for the steady RANS and 12000 time steps for the long-period DES. Contours of heatshield pressure coefficient (C_P) in Figs. 13a/13d show that DES gives a slightly higher mean pressure over the entire heatshield, which can be inferred from the shifted contour lines. The increase is larger over the lower part of the heatshield, particularly in the two gaps between the lower three nozzles. The stagnation pressure coefficient (C_{P_0}) is a measure of the post-shock flow energy in terms directly relevant to C_P and vehicle load coefficients. The surface C_P is proportional to the local C_{P_0} minus the dynamic pressure of the velocity just outside the heatshield boundary layer. The C_{P_0} data on the $y = 0''$ plane, shown in Figs. 13b/13e, are reasonably similar for RANS and DES, except for the stronger concave region near the lowest jet plume in the DES solution. This appears to be an example of the more-oblique shock in the DES solution leading to greater C_{P_0} being passed on the toward the heatshield. C_{P_0} data on the $x = 32''$ plane between the bow shock and the heatshield, depicted in Figs. 13c/13f, shows that a region of elevated C_{P_0} is flowing toward the heatshield in the gaps between the lower plumes. Thus, differences in the bow shock shape lead to higher C_P on the lower region of the heatshield.

These flowfield data do not explain the elevated C_P in the DES solution over most of the central heatshield. The data on $y = 0''$ show that the post-shock C_{P_0} in this region is just slightly lower for DES (Figs. 13b/13e), and the TKE in this region is also relatively low (not shown). Thus, of the three proposed mechanisms, only the net effects of blockage and entrainment remains in contention. The DES plumes are deflected less by the freestream flow; seven of the eight DES plumes reach the $x = 32''$ plane, while only five of the RANS plumes do. This may have the effect of 'funneling' more mass-flow into the region inside the ring of the jets.

Mechanisms that further affect the heatshield pressure are yet not well understood. Heatshield C_P is determined by C_{P_0} minus the dynamic pressure of outflow radial velocity, and the total velocity magnitude (V_{mag}) are given on the plane $x = 34.2''$ in Fig. 14, which is just ahead of the apex of the heatshield. The RANS solution give a higher V_{mag} closer to the plumes of $V_{mag} \sim 0.5$, while the DES solution yields a lower $V_{mag} \sim 0.4$. This assessment is approximate because the V_{mag} is not the V_{mag} normal to the jet, which would be a better measure of the entrainment rate. However, this result suggests that the RANS plumes are entraining air at a higher rate, which would act to lower C_P on the heatshield.

Thus, two of the proposed three mechanisms appear to be significant to the difference in C_D predicted with RANS and DES. The root cause of the difference appears to be lower turbulence in the DES plumes, as characterized by lower entrainment into shear layers and plume spreading. The DES plumes penetrate further upstream and result in a larger oblique area of the bow shock. The reduced entrainment also acts to increase the heatshield pressure. Comparison to

experimental data is required to further clarify the merits of these turbulence modeling techniques, but the differences can be use to quantify an uncertainty in drag prediction of up to ±7.5% for the OVERFLOW HIAD SRP CFD.

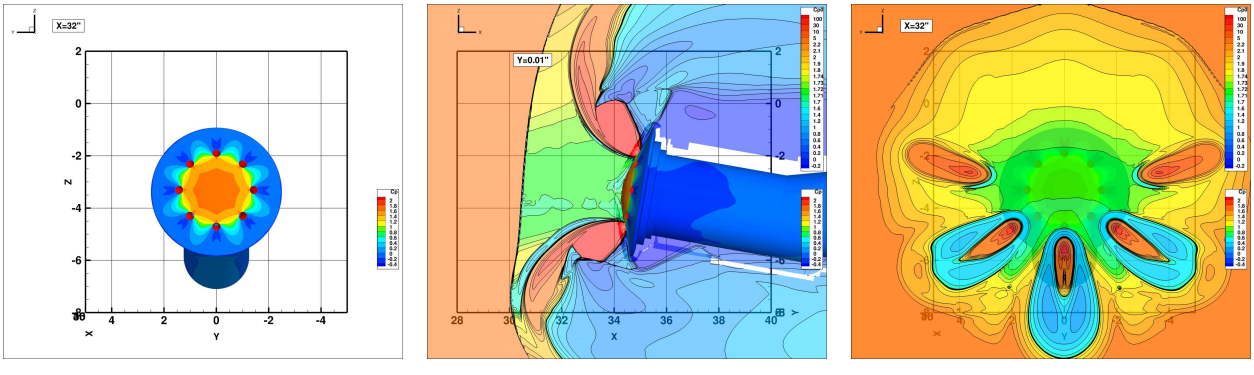

(a) Surface C_p, RANS (b) C_{P_0} on the $y = 0''$ plane, RANS (c) C_{P_0} on the $x = 32''$ plane, RANS

(d) Surface C_p, DES (e) C_{P_0} on the $y = 0''$ plane, DES (f) C_{P_0} on the $x = 32''$ plane, DES

Fig. 13 Comparisons of RANS and DES data: heatshield surface $C_P$and C_{P_0}on slices at $y = 0''$ and $x = 32''$ between the bow shock and heatshield ($M = 2.386$, $\alpha = 10°$ and $C_T = 2.5$)

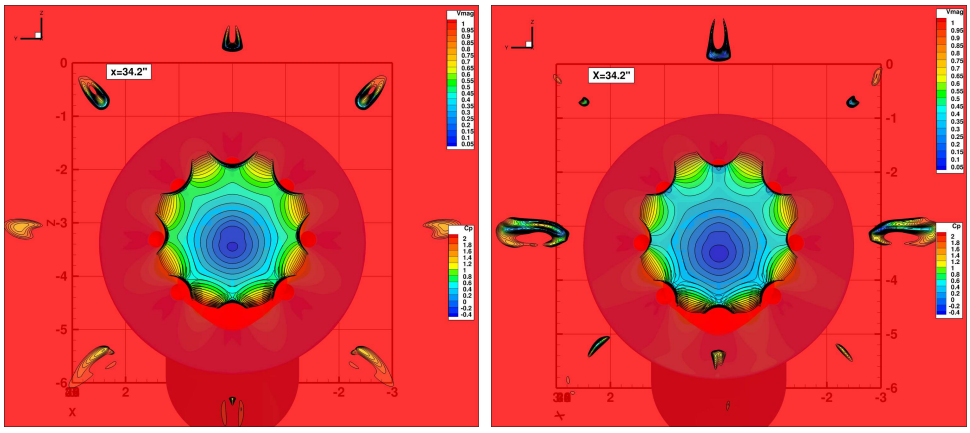

(a) C_{P_0}on the plane $x = 32''$ plane, RANS (b) C_{P_0}on the plane $x = 32''$ plane, DES

Fig. 14 Comparison of RANS and DES data: velocity magnitude on the plane $x = 34.2''$ just ahead of the heatshield ($M = 2.386$, $\alpha = 10°$ and $CT = 2.5$)

D. Vehicle Aerodynamic Performance

A comparison of the preliminary stability characteristics of different HIAD nozzle configurations can be accomplished by observing $\frac{dC_m}{d\alpha}$ trends in Fig. 15, where pitching moment coefficient (C_m) about the vehicle center of gravity (with $\frac{x_{cg}}{D} = 0.3$) is plotted. The 1E and 1F nozzle configurations both have a restorative $\frac{dC_m}{d\alpha} < 0$ at lower α, but this trend reverses for the model 1F at the highest tested α. Inferior performance of the 1F at high α and inconsistent performance at low thrust due to unsteady shock-plume interaction as observed in Section V.B make the 1E a potentially better choice for controllable atmospheric entry. It should be noted that these moments account for the loads on the forward heatshield only, as the wind tunnel sting interferes with the base flow of the blunt-body, and full-body aerodynamic loads may differ in trend from these results.

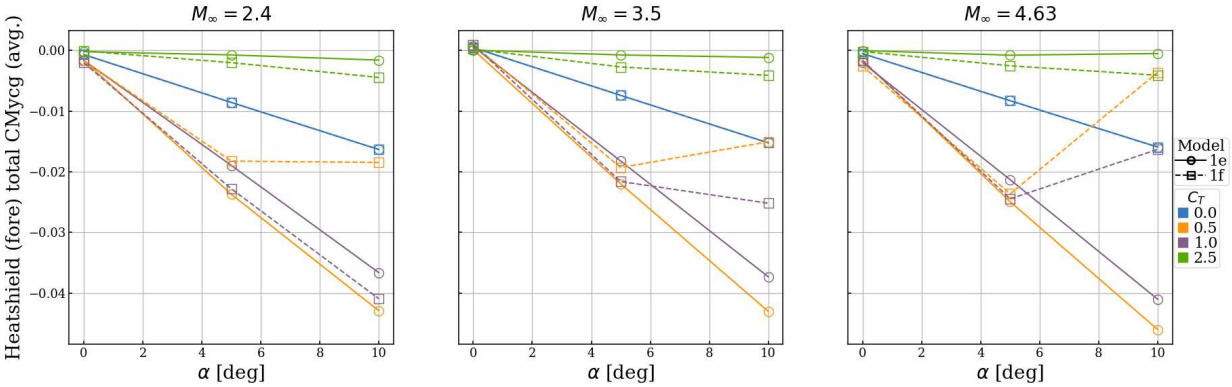

Fig. 15 Pitching moment about the center of gravity of various HIAD configurations

It is also important to consider the effectiveness of the vehicle as an aerodynamic decelerator for the Mars EDL mission. For the HIAD geometry, a significant amount of deceleration is achieved from the reverse thrust of SRP, but the aerodynamic C_D of the heatshield, shown in Fig. 16, is also an important contributor that must be accounted for. The 1E configuration tends to have notably more body drag for a given amount of thrust, and, in addition, the 1F configuration has a drag reversal at the highest C_T. These characteristics indicate that the 1E should perform better at the Mars EDL task, based on the data from this simulation alone.

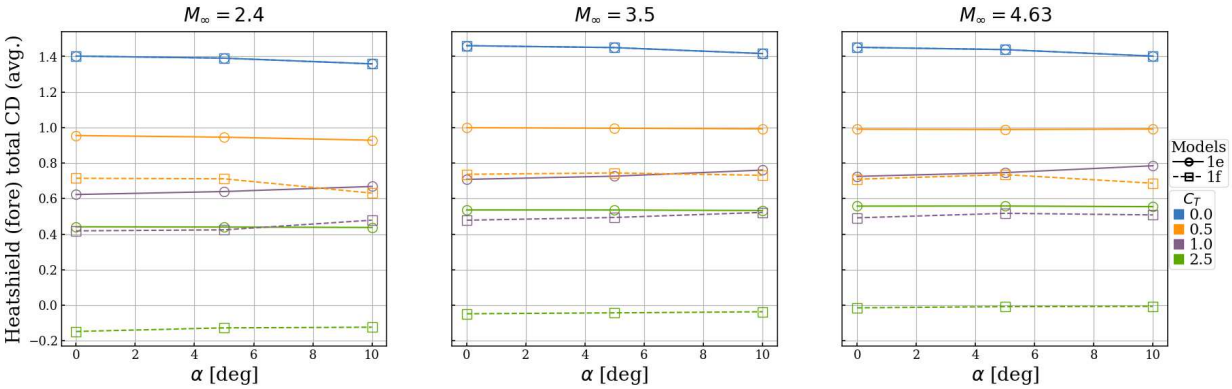

Fig. 16 Drag performance of various HIAD configurations

VI. Conclusion

This paper presented the preliminary analysis of supersonic retropropulsion over a blunt Mars EDL vehicle using OVERFLOW CFD solutions. A generalized, adaptive shock capturing and plume refinement methodology was developed and calibrated in order to produce automatically optimized overset SRP grid systems for a variety of testing conditions. Simulations of the HIAD 1E configuration were steady for all test conditions, while the 1F configuration tended towards unsteady, periodic oscillations of the plume and shock at low thrust, high angle of attack conditions. A preliminary investigation into turbulence modeling effects demonstrated that there is a significant difference of up to $\Delta C_D = 15\%$ in the estimated body drag between simulations modeled with RANS and DES, for some flight conditions. Two flow mechanisms were identified in the DES simulations as significant contributors to this difference: higher post-shock stagnation pressure due to augmented bow shock shape and reduced entrainment in the shear layers due to lower turbulence. Further investigation by comparison to experiment is required to discern which methodology is more capable of realistically approximating the average behavior of this SRP flow, but the relative differences between simulation techniques can be used to quantify the current CFD drag prediction uncertainty for these OVERFLOW simulations as up to $\pm 7.5\%$. Both HIAD nozzle configurations simulated showed similar C_m trends during SRP at low angle of attack, but the performance of the 1E was more consistent throughout the range of test conditions while the 1F C_m trend diverged at high angle of attack. The 1E configuration also had consistently greater magnitude body drag for a given thrust coefficient than the 1F.

In future, post-test simulations, further attention is needed in resolving the time-accurate behavior in these flows. The small subset of cases that were unsteady and non-periodic might be better modeled with a reduced time step or increased sub-iterations. If DES is shown to improve the fidelity of turbulence modeling in this SRP simulation, it should be applied to the full range of conditions (if feasible given realistic computational resource constraints) as it may more accurately represent unsteadiness in the blunt-body wake. Finally, better models of the wind tunnel test section inflow boundary conditions will be available and should help address uncertainty quantification in the current simulations.

Acknowledgments

This work is supported by the joint effort between NASA's Aerosciences Evaluation and Test Capabilities (AETC) program office under the Aeronautics Research Mission Directorate and the Game Changing Development Program (GCDP)'s Descent System Study (DSS) under the Space Technology Mission Directorate (STMD). CFD simulations were run on NASA Advanced Supercomputing Division resources and were funded by the GCDP's DSS. The authors thank the AETC and DSS teams for their advice and review of research.

References

[1] Cianciolo, A., Korzun, A., Samareh, J., Sostaric, R., Calderon, D., and Garcia, J., "Human Mars Entry, Descent, and Landing Architecture Study: Phase 3 Summary," 2020.

[2] Cerimele, C. J., Robertson, E. A., Sostaric, S. R., Campbell, C. H., Robinson, P., Matz, D. A., Stachowiak, S. J., Garcia, J. A., Bowles, J. V., Kinney, D. J., and Theisinger, J. E., "A rigid mid-lift-to-drag ratio approach to human Mars entry, descent, and landing," *AIAA Guidance, Navigation, and Control Conference*, 2017, p. 1898.

[3] Cianciolo, A. D., Dillman, R., Brune, A., Lugo, R., Polsgrove, T., Percy, T. K., Sutherlin, S., and Cassell, A., "Human Mars Entry, Descent and Landing Architecture Study: Deployable Decelerators," *AIAA SPACE*, 2018.

[4] Polsgrove, T., Dwyer-Cianciolo, A. M., Robertson, E. A., Percy, T. K., Samareh, J., Garcia, J., Lugo, R., Sostaric, R., Cerimele, C., and Garcia, J. A., "Human Mars Entry, Descent, and Landing Architecture Study: Rigid Decelerators," *2018 AIAA SPACE and Astronautics Forum and Exposition*, 2018, p. 5192.

[5] Calderon, D., Sostaric, R. R., Garcia, J. A., Bowles, J., Gaytan, C., Newton, H., Amar, J., and Wiens, Z., "Structural Mass Optimization with Manifest Packaging, and Outer Mold Line Updates of a Rigid Mid Lift-to-Drag Mars Entry Lander Vehicle," *AIAA Scitech 2020 Forum*, 2020, p. 1511.

[6] Ross, J. C., Rhode, M. N., Falman, B., Edquist, K., Schoenenberger, M., Brauckmann, G. J., Kleb, W. L., West, T., Alter, S. J., and Witte, D., "Evaluation of CFD as a Surrogate for Wind-Tunnel Testing for Mach 2.4 to 4.6-Project Overview," *AIAA AVIATION 2021 FORUM*, 2021, p. 2961.

[7] Matsuno, K., Childs, R., Pulliam, T., Stremel, P., and Garcia, J., "OVERFLOW Analysis of Supersonic Retropropulsion Testing on the CobraMRV Mars Entry Vehicle Concept," *Submitted to AIAA Scitech 2022 Forum*, 2022.

[8] Edquist, K. T., "Status of Mars Retropropulsion Testing in the Langley Unitary Plan Wind Tunnel," *Submitted to AIAA Scitech 2022 Forum*, 2022.

[9] Edquist, K. T., Alter, S. J., Glass, C. E., Kleb, B., Korzun, A. M., Wood, W. A., Canabal, F., Childs, R. E., Halstrom, L. D., and Matsuno, K. V., "Computational Modeling of Mars Retropropulsion Concepts Tested in the Langley Unitary Plan Wind Tunnel," *Submitted to AIAA Scitech 2022 Forum*, 2022.

[10] Edquist, K. T., Korzun, A. M., Kleb, W. L., Hawke, V., Rizk, Y. M., Olsen, M. E., and Canabal, F., "Model Design and Pre-Test CFD Analysis for a Supersonic Retropropulsion Wind Tunnel Test," *AIAA Scitech 2020 Forum*, 2020, p. 2230.

[11] Buning, P. G., "NASA OVERFLOW CFD Code," `https://overflow.larc.nasa.gov/`, 2021. Accessed: 2021-05-20.

[12] Buning, P. G., Jespersen, D. C., Pulliam, T. H., Chan, W., Slotnick, J. P., Krist, S., and Renze, K. J., "Overflow user's manual," *NASA Langley Research Center, Hampton, VA*, 2002.

[13] Nichols, R., Tramel, R., and Buning, P., "Solver and turbulence model upgrades to OVERFLOW 2 for unsteady and high-speed applications," *24th AIAA Applied Aerodynamics Conference*, 2006, p. 2824.

[14] Nichols, R. H., and Buning, P. G., "User's Manual for OVERFLOW 2.1," *University of Alabama and NASA Langley Research Center*, 2008.

[15] Rogers, S., Roth, K., Nash, S., Baker, M., Slotnick, J., Whitlock, M., and Cao, H., "Advances in overset CFD processes applied to subsonic high-lift aircraft," *18th Applied Aerodynamics Conference*, 2000, p. 4216.

[16] Chan, W., "The overgrid interface for computational simulations on overset grids," *32nd AIAA Fluid Dynamics Conference and Exhibit*, 2002, p. 3188.

[17] Chan, W., "Developments in Strategies and Software Tools for Overset Structured Grid Generation and Connectivity," *20th AIAA Computational Fluid Dynamics Conference*, 2011, p. 3051.

[18] Meakin, R., "Object X-rays for cutting holes in composite overset structured grids," *15th AIAA Computational Fluid Dynamics Conference*, 2001, p. 2537.

[19] Chan, W. M., Kim, N., and Pandya, S. A., "Advances in domain connectivity for overset grids using the x-rays approach," 2012.

[20] Menter, F. R., "Two-equation eddy-viscosity turbulence models for engineering applications," *AIAA journal*, Vol. 32, No. 8, 1994, pp. 1598–1605.

[21] Childs, R., Garcia, J., Melton, J., Rogers, S., Shestopolov, A., and Vicker, D., "Overflow Simulation Guidelines for Orion Launch Abort Vehicle Aerodynamic Analyses," *29th AIAA Applied Aerodynamics Conference*, 2011, p. 3163.

[22] Childs, R. E., Garcia, J. A., Rogers, S. E., and Vicker, D. J., "Overflow Aerodynamic Simulation of the Orion Launch Abort Vehicle," *Joint Army Navy NASA Air Force*, 2013.

[23] Mani, M., Babcock, D., Winkler, C., and Spalart, P., "Predictions of a supersonic turbulent flow in a square duct," *51st AIAA Aerospace Sciences Meeting including the New Horizons Forum and Aerospace Exposition*, 2013, p. 860.

[24] Spalart, P. R., "Strategies for turbulence modelling and simulations," *International journal of heat and fluid flow*, Vol. 21, No. 3, 2000, pp. 252–263.

[25] Childs, R., Stremel, P., Hawke, V., Garcia, J., Kleb, W. L., Hunter, C., , Parikh, P., Patel, M., Alter, S. J., Rhode, M. N., and Salari, K., "Flow Characterization of the NASA Langley Unitary Plan Wind Tunnel, Test Section 2: Computational Results," *AIAA AVIATION 2021 FORUM*, 2021, p. 2963.

[26] Buning, P. G., and Pulliam, T. H., "Near-body grid adaption for overset grids," *46th AIAA Fluid Dynamics Conference*, 2016, p. 3326.

[27] Berry, S. A., Rhode, M. N., and Edquist, K. T., "Supersonic Retropropulsion Experimental Results from NASA Ames 9× 7 Foot Supersonic Wind Tunnel," *Journal of Spacecraft and Rockets*, Vol. 51, No. 3, 2014, pp. 724–734.

[28] Schauerhamer, D. G., Zarchi, K. A., Kleb, W. L., Carlson, J.-R., and Edquist, K. T., "Supersonic Retropropulsion Computational Fluid Dynamics Validation with Langley 4× 4 Foot Test Data," *Journal of Spacecraft and Rockets*, Vol. 51, No. 3, 2014, pp. 693–714.

VII. Appendix

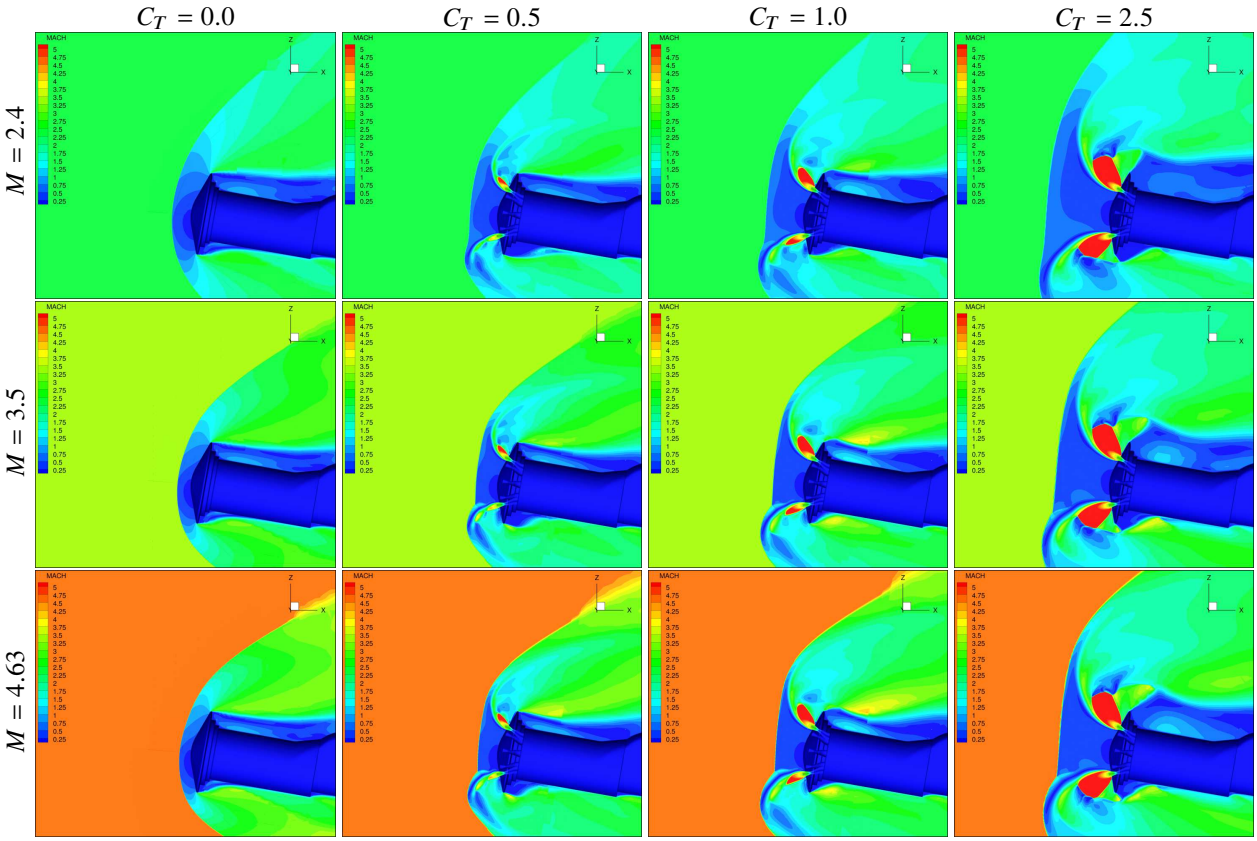

Fig. 17 Mach number contours for HIAD 1E at $\alpha = 80°$ as a function of tunnel condition and thrust coefficient